Normal-Mode Theory Applied to Short-Range Propagation in an Underwater Acoustic Surface Duct

MELVIN A. PEDERSEN AND DAVID F. GORDON

U. S. Navy Electronics Laboratory, San Diego, California 92152

(Received 25 September 1964)

This paper presents detailed numerical comparisons between propagation losses as calculated by ray theory and by mode theory. Both theories are based on the bilinear surface-duct model. In the image-interference region, the theories give almost identical results, the accuracy of the mode solution being limited at very close ranges by the number of modes treated. As many as 40 modes are considered. Comparison with experimental data at 530 and 1030 cps indicates that the mode theory is definitely superior to ray theory in regions where ray theory predicts shadow zones and caustics. The nature of the mode solution is examined in detail. The manner in which the mode theory produces the image-interference pattern is controlled by the detailed amplitude and phase characteristics of a large number of modes and is not readily interpreted as the interference between a direct and a surface-reflected acoustic path.

INTRODUCTION

THIS paper presents the results of normal-mode theory as applied to short-range propagation of underwater sound in a surface duct (ranges less than 10 kyd). The normal-mode approach to surface ducts was applied to electromagnetic propagation by Furry[1] and later applied to underwater sound by Marsh.[2] Their interest was limited to a few modes at long range where ray theory breaks down. Our initial interest was to determine whether this mode theory could be extended to short ranges and overlap the region where ray theory applies, or whether there was a gap at intermediate ranges where neither theory was accurate.

With suitable improvements and corrections to the original approach, we have been able to apply normal-mode theory at short ranges in the image-interference region where ray theory is known to be valid. As is shown, there are range intervals over which the propagation losses of mode theory and ray theory are for all practical purposes identical. Thus, there is no range gap between valid solutions and, as a result, the whole normal-mode approach, which is exceedingly complicated and detailed as compared to ray theory, is substantiated. Furthermore, a comparison with experimental data at frequencies of 530 and 1030 cps indicates that the normal-mode-theory approach is definitely superior to ray theory at the somewhat longer ranges where ray theory predicts shadow zones and caustics.

Section I of this paper presents the normal-mode and ray-theory solutions. Section II compares these solutions with experimental propagation-loss data. Section III presents intermediate results of the mode theory, chosen to illustrate the nature of the solution in more detail.

All of the theoretical calculations appearing in this paper were made on a CDC-1604 computer.

I. THEORETICAL SOLUTIONS

In this section, some of the basic expressions necessary for the calculation of propagation loss are presented. We shall not treat derivations or the intricate mathematical problems that arise in the numerical evaluation of the functions that appear in the normal-mode solution.

A. Velocity-Depth-Profile Model

Both theories are based on the bilinear-gradient model of a surface channel, as shown in Fig. 1. The nomenclature for the model stems from the linear nature

---

[1] W. H. Furry, "Theory of Characteristic Functions in Problems of Anomalous Propagation," Mass. Inst. Technol. Lab. Rept. 680 (1945); "Methods of Calculating Characteristic Values for Bilinear *M* Curves," *ibid.* Rept. 795 (1946).

[2] H. W. Marsh, "Theory of the Anomalous Propagation of Acoustic Waves in the Ocean," U. S. N. Underwater Sound Lab. Rept. 111 (1950).
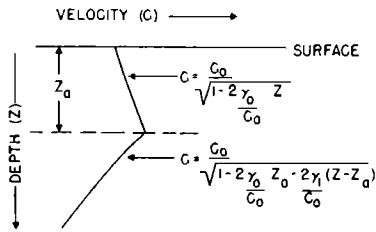
FIG. 1. Bilinear-gradient model of a surface channel.

of the index of refraction. The velocity profile consists of two curvilinear functions having the form as shown. In practice, these functions are very close to straight lines. This particular mathematical form is selected because the depth-dependent portion of the wave equation reduces exactly to Stokes' equation upon separation of the range and depth variables. Z_a is the depth of the channel, C_0 is the surface velocity, and γ_0 and γ_1, respectively, are measures of the gradient in and below the channel. In the general mode theory, γ_1 is negative, whereas γ_0 may be either positive or negative. This paper considers only the case of γ_0 positive—the condition for a surface sound channel.

There are three additional basic parameters that are determined by the experimental setup. These include the frequency f and the source and receiver depths, designated by Z_0 and Z, respectively.

B. Normal-Mode Solution

The general treatment follows Marsh,[2] with certain corrections, modifications, and extensions. For the present, those interested in derivations should consult Marsh[2] or Furry.[1] It should be noted, however, that Marsh[2] contains a considerable number of typographical errors that make comparison difficult with the solution presented here.

Before presenting the solution, let us point out some of the procedures necessary in the extension of Marsh's treatment (valid for long ranges) to short ranges. At long range, only a few low-order modes need be treated, whereas at short range many modes must be included. The eigenvalues for low-order modes were obtained by Marsh and Furry using certain asymptotic approximations. Since these approximations are not valid for higher-order modes, our approach must find the roots of the eigenvalue equation itself. Marsh and Furry also used asymptotic expansions that were valid only at long ranges. In contrast, our approach avoids mathematical approximations and all expressions are computed with as much accuracy as is feasible, using single-precision arithmetic.

Certain useful combinations of the basic parameters, given in the previous section, are

$$t = Z/Z_a, \quad t_0 = Z_0/Z_a, \quad \rho = (\gamma_0/\gamma_1)^{\frac{1}{3}}, \quad k = 2\pi f/C_0, \quad (1)$$

and $M = (2k^2\gamma_0/C_0)^{\frac{1}{3}}Z_a$. Here, the real cube roots are taken. M is a dimensionless parameter that is a measure of the strength of the channel.

In this theory, the source and receiver depths are interchangeable; i.e., reciprocity holds. A set of major items necessary in the computation are the depth functions $U_n(t)$, where the subscript n indicates the mode number. These functions indicate the degree to which the mode excites (or is excited by) a particular receiver (source) at the particular depth. As we see later, these depth functions may be regarded as mode amplitudes before any dependence on range is considered. These depth functions are complex and, hence, contain phase information as well as amplitudes in the usual sense. When Marsh's[2] equations are evaluated in detail, the following form results for the product of the depth functions:

$$U_n(t)U_n(t_0) = (M/Z_a)F_n(t)F_n(t_0)/D_n. \quad (2)$$

D_n is presented later. $F_n(t)$ takes one of two forms as follows:

Case I: When $t \leq 1$, corresponding to the receiver (source) in the channel,

$$F_n = \mathcal{Q}(t). \quad (3a)$$

Case II: When $t \geq 1$, corresponding to the receiver (source) below the channel,

$$F_n = \mathcal{Q}(1)h_2(B_t)/h_2(B_1). \quad (3b)$$

The function $\mathcal{Q}(t)$ and the argument B_t in (3a) and (3b) are given by

$$\mathcal{Q}(t) = h_1(Mx_n)h_2(Mx_n - Mt) - h_2(Mx_n)h_1(Mx_n - Mt) \quad (4)$$

and

$$B_t = \rho^2(Mx_n - M) + (M - Mt)/\rho. \quad (5)$$

$\mathcal{Q}(1)$ and B_1 are obtained by setting $t = 1$ in (4) and (5). Expressions for $F_n(t_0)$ are obtained by replacing t by t_0 in Eqs. (3)–(5).

The h_1 and h_2 functions in Eqs. (3) and (4) are complex solutions of Stokes' equation and are referred to as modified Hankel functions of order one-third. These functions are computed by methods discussed by the Harvard Computational Laboratory.[3] First derivatives of these functions are designated as h_1' and h_2'.

The quantity Mx_n in Eqs. (4) and (5) is a complex eigenvalue and is a root of the characteristic equation

$$G = \rho h_2(B_1)\beta - h_2'(B_1)\mathcal{Q}(1) = 0, \quad (6)$$

where

$$\beta = h_1(Mx_n)h_2'(Mx_n - M) - h_2(Mx_n)h_1'(Mx_n - M). \quad (7)$$

Marsh treats the quantity x_n as a separate entity. This separation seems unnecessary as x_n always appears with M as a multiplier.

Equation (6) has an infinite number of roots, each

---

[3] *Tables of the Modified Hankel Functions of Order One-Third and of Their Derivatives* (Harvard University Press, Cambridge, Mass., 1945).

root corresponding to a normal mode. In the case treated here, the first mode corresponds to the root with the smallest real and imaginary parts, the second mode to the next larger real and imaginary parts, etc. Hence, the modes may be ordered by either RelMx_n or ImMx_n. We have investigated other cases where the numbering of modes is ambiguous. In the case of γ_0 negative, a different ordering is obtained from a consideration of RelMx_n than from consideration of ImMx_n. Another complication in ordering, which arises for small γ_1 is the appearance of an additional set of modes, entirely distinct from the set treated in this paper.

Equation (6) is solved by Newton's method in the complex plane. In brief, for the lowest-order modes, initial values for Newton's method are obtained from certain asymptotic approximations. For higher-order modes, initial values are obtained by extrapolation based on the three next-lower-order eigenvalues. The function D_n in (2) is given by

$$D_n = (\rho^3 - 1)[\beta^2 + (Mx_n - M)\mathcal{Q}^2(1)] - 2.124292605, \quad (8)$$

where the negative constant is the square of the Wronskian $W(h_1,h_2)$.

We now have presented all the expressions necessary to calculate the depth functions of (2) and are ready to introduce the range dependence. The propagation loss H is given as a function of range r by

$$H = -10 \log \left| \sum_1^N H_0{}^2(\lambda_n r) U_n(t) U_n(t_0) \right|^2 \\ - 20 \log \pi + \alpha_A r. \quad (9)$$

$H_0{}^2$ is the second Hankel function of order zero. The term λ_n is complex and is given by

$$\lambda_n = [k^2 - Mx_n(M/Z_a)^2]^{\frac{1}{2}}. \quad (10)$$

The complex square root is taken so that λ_n lies in the fourth quadrant. N is the number of modes included in the computation. It is not always evident what this number should be but, as is shown later in an example, the number of modes required in the computation increases with decreasing range.

The result of the summation in (9) is complex. Hence, this complex number is changed to an absolute value before computing the logarithm. The item $\alpha_A r$ in (9) has nothing to do with normal-mode theory but represents the effect of physical absorption and scattering. If units of yards are used for all length dimensions throughout the computation, then H represents the decibel loss relative to 1 yd, with no additional scaling being necessary.

There are three important aspects of this normal-mode approach that contrast to many other normal-mode solutions to the wave equation: (1) The solution is valid even for short ranges, because the branch-line integral, often present in a complete solution, is zero

for this model. (2) λ_n is a complex wavenumber and therefore the modes are damped. (3) There are no cutoffs in the frequency domain. Hence, in theory, an infinite number of modes must be treated, but in practice the higher-order modes are so highly damped that they contribute only at extremely short ranges.

Before continuing, we should note that the problem of the branch-line integral is an exceedingly complicated one and has not been investigated in detail by the authors. In a private communication, Marsh has indicated that the integral is zero for this model. This is demonstrated in some detail by Towne and Wilson[4] for the single layer case ($Z_a = 0$). Furthermore, according to Stone[5] the appearance of a branch-line integral is only a consequence of the fact that the medium is unbounded in the Z direction and is not associated with boundary conditions at layer interfaces. Thus, we may conclude that the nature of the velocity profile in the infinite layer determines the presence of a branch-line integral. This view is substantiated by Towne and Wilson,[4] who state that the existence of branch points is associated with the fact that $C(Z)$ does not vanish at infinity. For the model of Fig. 1, $C(Z)$ does indeed vanish at infinity.

C. Simplified Form of the Mode-Theory Solution

The preceding section gives the rigorous and accurate mathematical expressions that are used in the actual computational work. However, these exact expressions are not readily interpreted. In contrast, this section discusses certain simplifying approximations that present an excellent qualitative description of the theoretical result and that can be readily understood.

It is convenient to decompose the λ_n of (10) into the form

$$\lambda_n = k - \sigma_n - i\tau_n. \quad (11)$$

In general, $k \gg |\sigma_n|$ or τ_n.

We now investigate the significance of σ_n and τ_n in the propagation-loss equation. Using only the first term of the asymptotic expansion for $H_0{}^2(\lambda_n r)$, we find that H may be written as

$$H \sim -10 \log\left[\left(\sum_1^N A_n \cos\theta_n\right)^2 + \left(\sum_1^N A_n \sin\theta_n\right)^2\right] \\ - 10 \log(C_0/f) + 10 \log r + \alpha_A r, \quad (12)$$

where

$$A_n = |U_n(t)U_n(t_0)| \exp(-\tau_n r), \quad (13)$$

$$\theta_n = \Psi_n + \sigma_n r, \quad (14)$$

[4] D. H. Towne and K. G. Wilson, "Refraction and Diffraction of Explosive Pressure Pulses by Gradients in the Propagation Velocity," Pt. II, Woods Hole Oceanog. Inst. Ref. No. 57–45 (1957).

[5] J. L. Stone, "A Theoretical Analysis of Acoustic Wave Modes in Layered Liquids," Princeton Univ. Rept. No. 9, contract N6ONR–270 (1953).
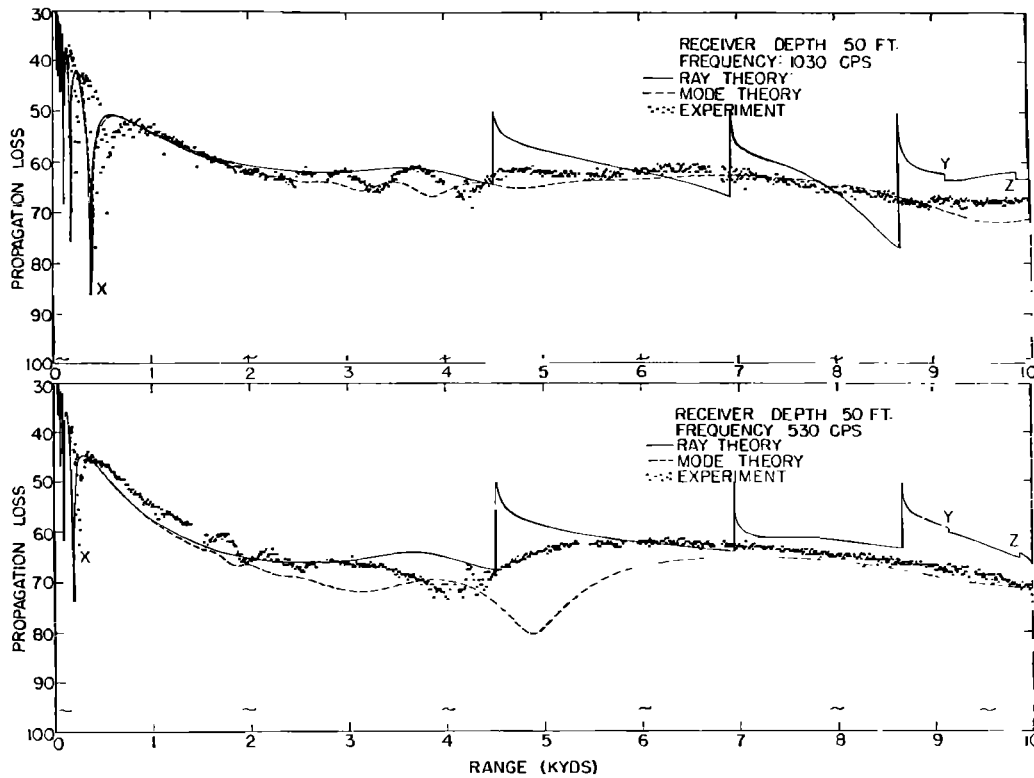
FIG. 2. Propagation losses for 50-ft receiver, 55-ft source.

and

$$\Psi_n = \arg\{U_n(l)U_n(l_0)\}. \tag{15}$$

The 10 log$r$ term of (12) corresponds to cylindrical spreading and represents the general trend with range. Superimposed on this general trend is the interaction between the modes. These modes may be thought of as damped sinusoidal waves whose damped amplitude and phase angles at range r are given by A_n and θ_n, respectively.

The value of a given A_n relative to the values of the other A_n's determines the extent to which a particular mode contributes to the final result. From (13), we see that there are two fundamentally different factors that determine how much a particular mode contributes to the result. The first, $|U_n(l)U_n(l_0)|$, depends on the source and receiver depth but not on range. The opposite is true of the second factor, $\exp(-\tau_n r)$. In describing the effect of range, it is necessary to note that τ_n always increases with increasing n. Thus, as the range increases, the relative contribution of a mode decreases with increasing mode number.

Now, it happens that k^2 is the dominant term in (10). A good approximation to λ_n is given by

$$\lambda_n \sim k - Mx_n(M/Z_a)^2/2k. \tag{16}$$

Thus,

$$\sigma_n \sim \Gamma \mathrm{Re} l M x_n \quad \text{and} \quad \tau_n \sim \Gamma \mathrm{Im} M x_n \tag{17}$$

with $\Gamma = (\pi f \gamma_a{}^2)^{\frac{1}{2}}/C_0$. From (17), we see that the mode

damping is determined primarily by the imaginary part of the eigenvalue, whereas the rate of change of phase with range is determined by the real part.

D. Ray-Theory Solution

In order to make a valid comparison between the mode theory and ray theory, the ray-theory approach must be based on the identical profile model of Fig. 1. In this section, the computing forms for a ray theory, based on the profile model

$$1/C^2 = a + bZ, \tag{18}$$

are presented.

The ray to be calculated is designated by the parameter C_m, the velocity at which the ray becomes horizontal. In this case, Snell's law becomes

$$\cos\theta_i = C_i/C_m, \tag{19}$$

where θ_i is the angle formed by the ray with the horizontal at interface i and C_i is the velocity at interface i. Then

$$\tan\theta_i = (C_m{}^2 - C_i{}^2)^{\frac{1}{2}}/C_i \tag{20}$$

and $\cot\theta_i$ is the reciprocal. (In this treatment, θ_i, itself, is never used so could be completely dispensed with. However, the notations $\tan\theta_i$ and $\cot\theta_i$ are physically meaningful and eliminate in the theoretical treatment the repeated use of the cumbersome forms by which they are actually computed.) Consider the

FIG. 3. Propagation losses for 232-ft receiver, 55-ft source.
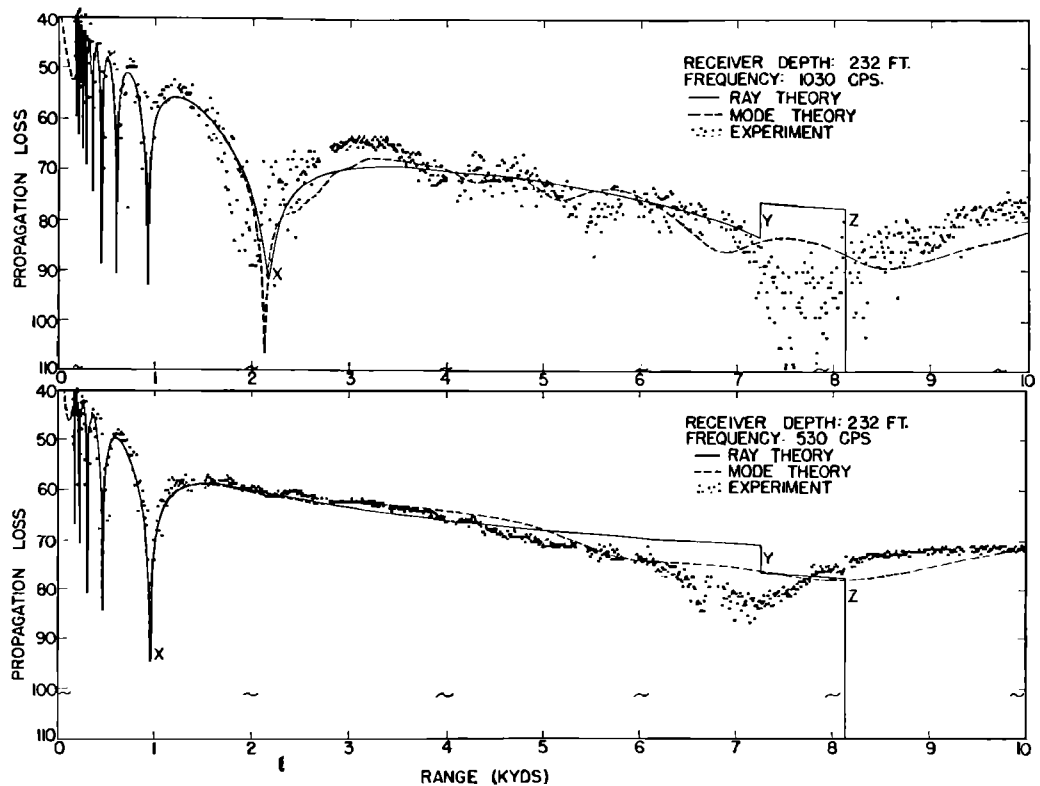
profile layers ordered with increasing Z and that the velocity at the upper and lower interfaces of layer i are C_i and C_{i+1}, respectively. The horizontal range in layer i in case the ray passes completely through the layer is

$$R_i = 2(\tan\theta_{i+1} - \tan\theta_i)/bC_m^2. \qquad (21)$$

The corresponding travel time is

$$T_i = 2(\tan^3\theta_{i+1} - \tan^3\theta_i)/3bC_m^3 + R_i/C_m. \qquad (22)$$

The corresponding derivative term, necessary in the intensity formulation, is

$$B_i \equiv C_m dR_i/dC_m = 2(\cot\theta_{i+1} - \cot\theta_i)/bC_m^2 - R_i. \qquad (23)$$

If the ray forms a nadir or an apex in the layer, then the first or second item in the parentheses of Eqs. (21)–(23) is omitted.

The complete range (R), travel time (T), and derivative (B) are obtained by summing expressions (21)–(23) over all layers as traversed along the ray path from source to receiver.

The ray intensity for a unit source is computed by the expression[6]

$$I/F = C_s |\cot\theta_s| |\cot\theta_h|/C_h RB, \qquad (24)$$

where s and h refer to the source and receiver interfaces,

[6] M. A. Pedersen, "Acoustic Intensity Anomalies Introduced by Constant Velocity Gradients," J. Acoust. Soc. Am. 33, 465–474 (1961).

respectively, and F indicates a measure of the source strength.

In the case of the ray that is horizontal at source or receiver, Eq. (24) is an indeterminate form. In this case, the general expressions given at the bottom of page 467 and top of 468 of Ref. 6 were used. Direct evaluation of the limit using (23) leads to the same result.

The propagation loss for the combination of n arrivals was calculated from

$$H = -10 \log\left\{\left[\sum_1^n \left(\frac{I_j}{F}\right)^{\frac{1}{2}} \cos\theta_j\right]^2 + \left[\sum_1^n \left(\frac{I_j}{F}\right)^{\frac{1}{2}} \sin\theta_j\right]^2\right\} + \alpha_A r. \qquad (25)$$

The phase angle is computed from

$$\theta_j = 2\pi f T_j + \pi P_j, \qquad (26)$$

where T_j is the travel time of arrival j and P_j is the number of times the arrival has reflected from the surface. It should be noted that (I_j/F) and T_j must be evaluated at the same range for all j, whereas for the various arrivals the values of T and I/F as initially computed fall at random ranges, depending on the selection of the ray parameters. Values of I_j/F and T_j for the desired ranges are determined by curvilinear
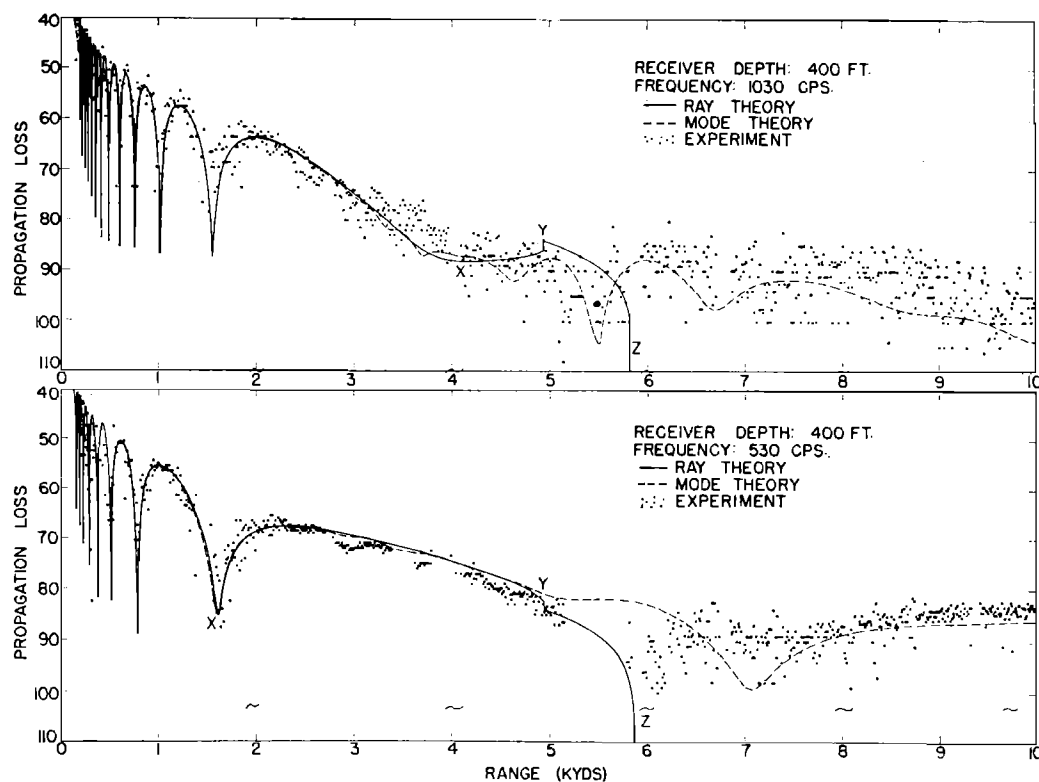
FIG. 4. Propagation losses for 400-ft receiver, 55-ft source.

interpolation based on the ray-theory computations for three successive values of the ray parameter. This complete process is done by computer, with the final output being propagation loss as a function of range.

II. COMPARISONS, THEORETICAL AND EXPERIMENTAL

In this section, we compare the ray- and mode-theory solutions with experimental results, the ray- and mode-theory solutions with each other, and the mode-theory solutions for two velocity profiles.

A. Comparison of Theories with Experiment

The experimental data are the same as discussed in a previous paper.[7] In brief, two sources (530- and 1030-cps frequency) were towed at depths of 55 ft. Signals were received on hydrophones at depths of 50, 232, and

TABLE I. Parameters for profiles taken at the source (S.S.) and receiver (R.S.) ships.

	C_0(ft/sec)	Z_a(ft)	γ_0(sec^{-1})	γ_1(sec^{-1})
S.S	4940.94	326.67	0.0144	−0.438
R.S.	4940.79	313.33	0.0114	−0.423

[7] M. A. Pedersen, "Comparison of Experimental and Theoretical Interference in Deep-Water Acoustics," J. Acoust. Soc. Am. 34, 1197–1203 (1962).

400 ft. Values of the mean profile parameters as determined from bathythermograph data taken at the two ships are given in Table I, which uses the notation of Fig. 1. Values of the gradient in the layer are significantly less than that of an isothermal layer, which is 0.0182 sec^{-1}.

Figures 2–4 present propagation loss as a function of range out to 10 kyd. Each dot in the experimental data represents measurements of an individual $\frac{1}{2}$-sec pulse transmission. The tilde marks near the bottom of Figs. 2–4 indicate the propagation loss corresponding to the average noise level. Both the ray-theory and mode-theory calculations are based on the source-ship profile of Table I. The ray-intensity computations were based on 78 ray parameters, including all critical rays such as the ray grazing the bottom of the surface layer. At 1030-cps frequency, 40 modes were included in the normal-mode calculations while at 530 cps only 29 modes were included. (The 40-mode figure arises from storage limitation in the computer; the 29-mode figure arises from exponent overflow in the computer when attempting to evaluate modes of higher order.) In both theoretical approaches, α_A was taken to be 0.0127 and 0.345 dB/kyd at 530 and 1030 cps, respectively.

The letter Z indicates the dropout of the surface reflected ray that grazes the bottom of the surface channel. Note that the intensity change at range Z is much more abrupt in Fig. 3 than in Fig. 4. This results
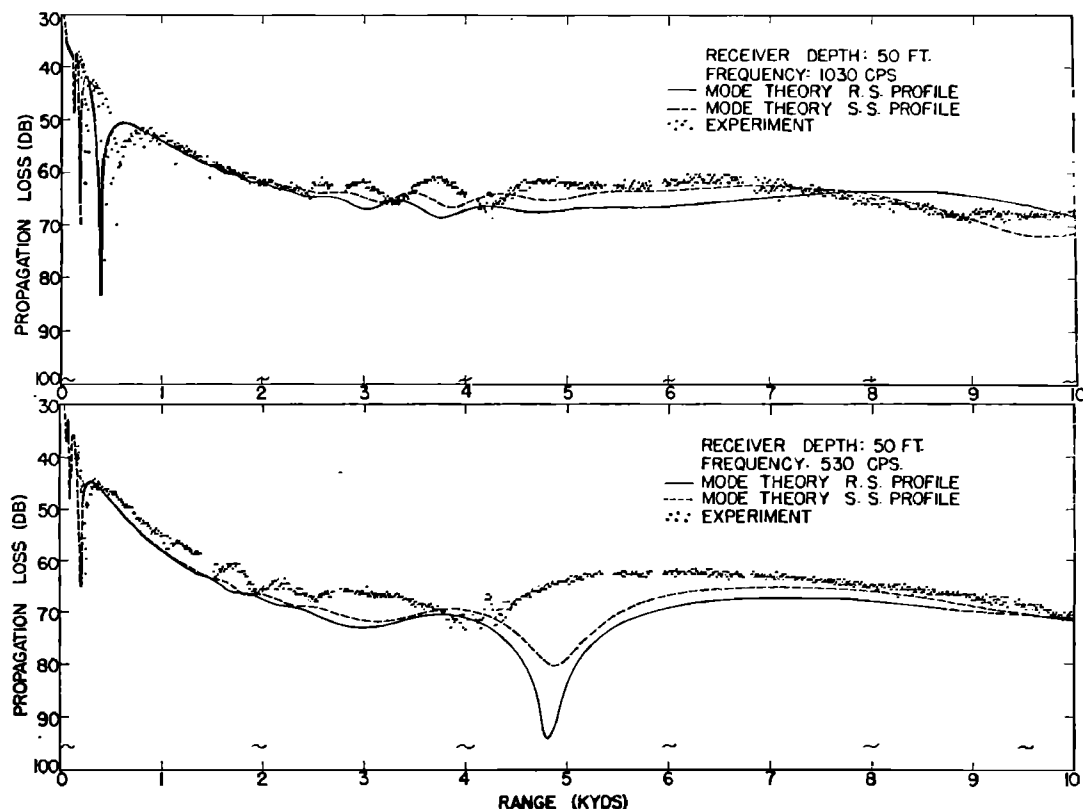
FIG. 5. Propagation losses for 50-ft receiver, 55-ft source.

from the fact that the slope discontinuity at the bottom of the channel does not affect the intensity of the limiting ray for a receiver in the channel. However, for a receiver below the layer, the discontinuity causes the intensity to go to zero in a continuous manner as the ray parameter approaches that of the limiting ray. The letter Y indicates the dropout of the direct ray, which grazes the bottom of the channel. The letter X indicates the range of the last null in the image interference pattern for ray theory. The discontinuities in the ray-theory calculation in Fig. 2, occurring at about 4.5, 6.9, and 8.7 kyd, are caustics, indicating the onset of additional arrivals. The minimum loss associated with these caustics has been arbitrarily terminated at 50 dB loss, although elementary ray theory yields infinite intensity at the caustic.

Note that, in all six examples given in Figs. 2-4, the mode-theory result is in better agreement with experiment than is the ray-theory result. In Fig. 2, there is no evidence of caustics or even convergence regions in the experimental data. For the 232-ft receiver of Fig. 3, ray theory predicts a shadow zone from 8.1 to 11.4 kyd. This contrasts to the experimental data in which the propagation losses are actually seen to be decreasing over the interval from 8 to 10 kyd. The mode theory shows such a decrease, but the last fade in the mode pattern is shifted out in range and is not as deep as the

corresponding experimental fades occurring between 7 and 8 kyd. However, this last experimental fade cannot be explained at all by simple image interference, since the last null of ray theory occurs at range X. In Fig. 4, a ray-theory shadow zone exists at ranges beyond 5.8 kyd, although there is no such indication in the experimental data. Agreement between mode theory and experiment beyond this range is fairly good for the 530-cps frequency. It is only fair at 1030-cps frequency. This feature is discussed later in a further comparison between mode theory and experiment when the results of the mode theory for a different profile are presented.

B. Comparison of Ray- and Mode-Theory Solutions

The ray and mode theories give almost identical results over certain range intervals, which vary somewhat with depth and frequency. At extremely short ranges (as, for example, $R < 500$ yd at 1030 cps in Fig. 4), there is considerable departure. As is shown later, this departure can be attributed to the omission of higher-order modes in the mode computation.

At short ranges then, agreement between mode and ray theory seems limited only by the number of modes that must be included. At somewhat longer ranges, where the rays are not so steep and where refraction
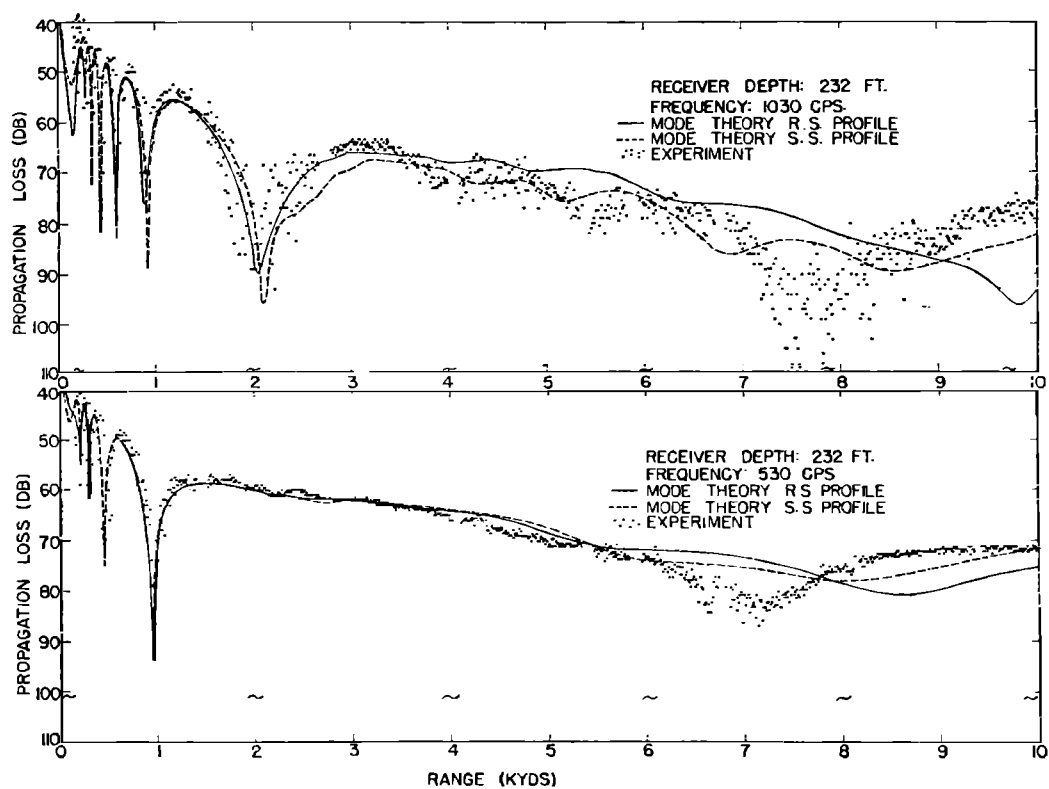
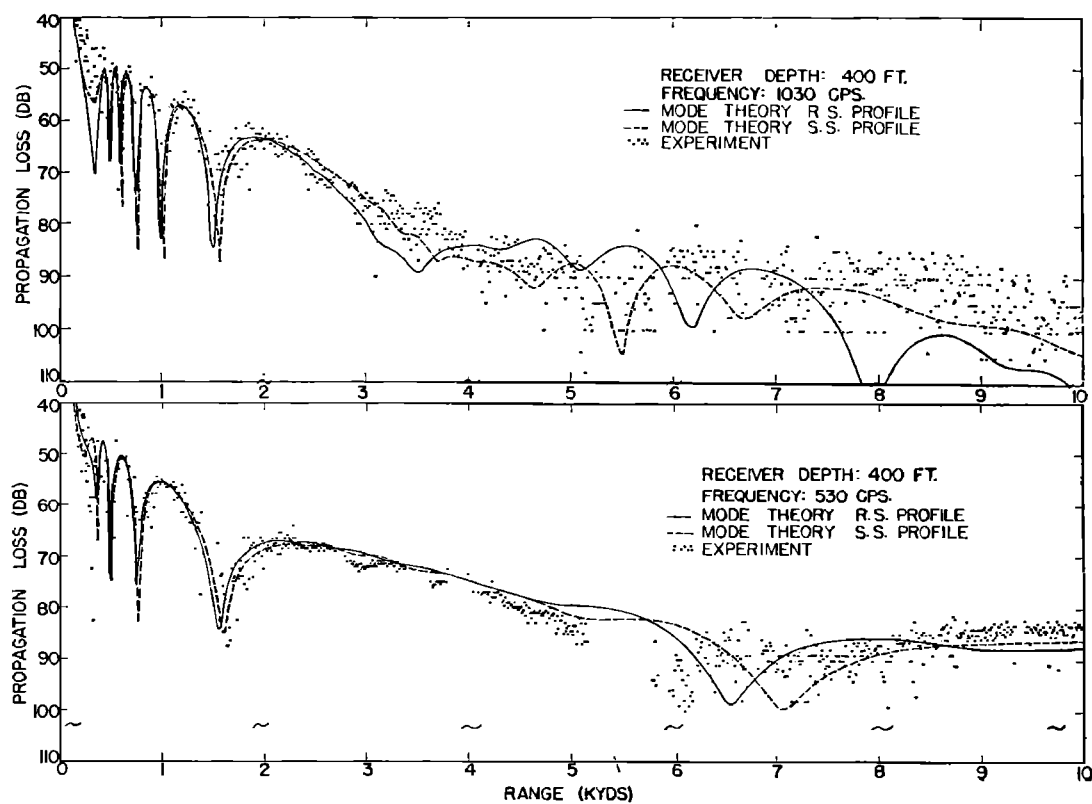FIG. 6. Propagation losses for 232-ft receiver, 55-ft source.

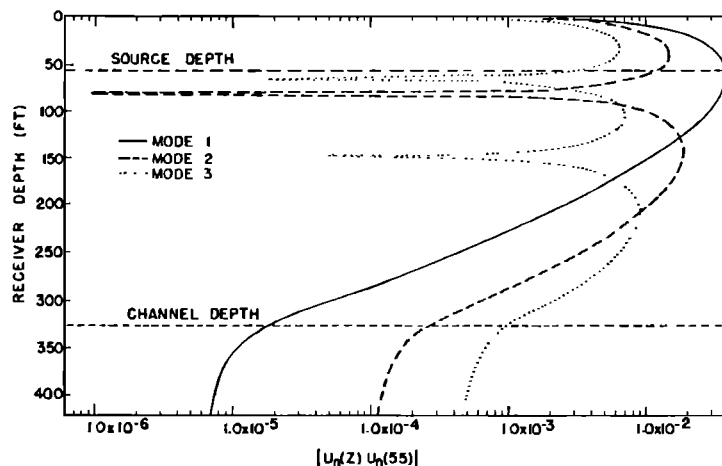FIG. 7. Propagation losses for 400-ft receiver, 55-ft source.

FIG. 8. Depth-function amplitude for modes 1–3 (1030 cps).

effects become more important, the solutions begin to depart. Note, however, in Figs. 3 and 4 that the solutions agree fairly well (the mode solution oscillating about the ray solution) clear out to the shadow zone where simple ray theory finally breaks down completely.

There are no shadow zones in Fig. 2. In this case, ray and mode theories are in substantial agreement until the ray-theory caustics appear. Beyond this range, the ray and mode theories show marked departures. Although the general level of propagation loss is comparable at 1030 cps, the mode-theory losses for 530 cps are systematically larger than the ray-theory losses. We believe that we could get better agreement between the ray and mode theories in the caustic region if we made the comparison for even higher frequencies as the ray-theory solution becomes a better approximation as the frequency is increased.

C. Comparison of Mode Theories for Two Profiles

Thus far, we have presented the mode-theory results for the source-ship profile. These results, as well as the

experimental data, are duplicated in Figs. 5–7. However, the solid line in this case is the normal-mode solution for the receiver-ship profile of Table I. For this profile, 40 modes were included at 1030 cps and 25 modes at 530 cps.

Note that the greatest difference between the mode solutions for the two profiles occurs in Fig. 7 for 1030 cps at ranges beyond 5 kyd. (Note also that this is a region of great fluctuation in the experimental data, indicating a critical dependence on environmental conditions.) With this exception, the solutions are quite comparable in that the chief difference in many cases is a slight range shift in the patterns. This and the results of other investigations, not reported here, indicate that the mode phase is more sensitive to slight profile changes than is the mode amplitude. Thus, the detailed interference patterns of mode theory and experiment are often quite similar but shifted somewhat in range.

In general, agreement between theory and experiment is comparable to the agreement between the
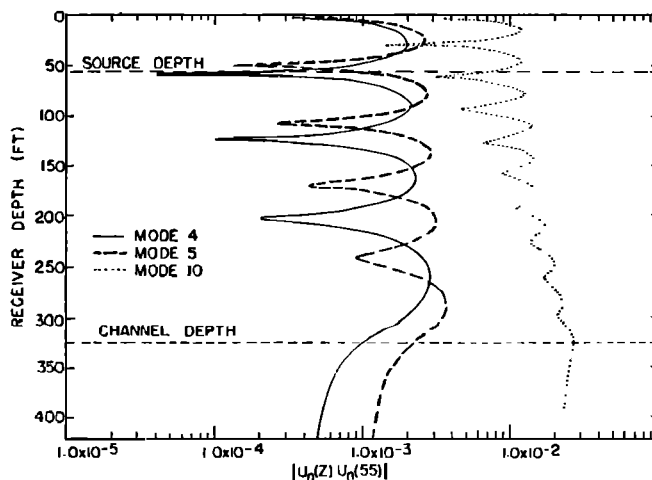

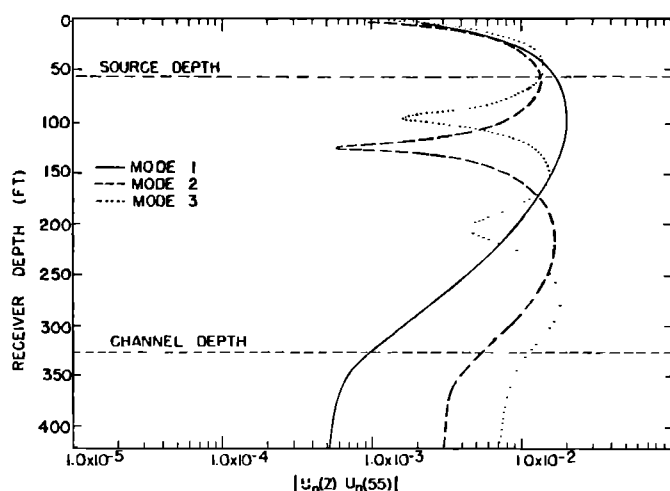FIG. 9. Depth-function amplitude for modes 4, 5, and 10 (1030 cps).

mode-theory solutions for the two profiles. There are, however, exceptions, the most noteworthy being the pronounced null that appears in Fig. 5 at 530 cps in both theoretical solutions at 4.8 kyd, with little evidence of such in the experimental data.

The degree of over-all agreement between experiment and theory is probably more than we have any right to expect. In the first place, the theory is based on the simple two-layer model of Fig. 1 whereas the BT data of experiment showed a definite three-layer condition, the extra layer having a negative gradient and extending from the surface to a depth of 30 ft (Ref. 7). Secondly, the BT data showed considerable temporal and spatial variability during the experiment whereas the theoretical calculation is based on a fixed "average" profile.

III. INTERMEDIATE MODE-THEORY RESULTS

As is well known, the image-interference pattern is subject to a simple physical interpretation. It is formed by the interaction between a surface-reflected path and a direct path. Indeed, methods based on this physical concept with the assumption of isovelocity water provide an approximation that contains the essential features.[7] The detailed ray-theory approach follows this same basic concept, but with embellishments to account for refraction effects.

One might suppose then that the image-interference pattern of mode theory is produced by a simple interaction between modes and is subject to a simple physical interpretation. The purpose of this section is to indicate that this is not the case and that, although the mode theory indeed produces the pattern, it does so in an exceedingly complicated manner. We present examples that indicate not only the contribution of indivudal modes but also the dependence of this contribution on depth and range. This provides considerable insight into the general nature of the mode solution.

A. Initial Mode Amplitude and Phase

Consider first the dependence of the mode solution on the depth variable for profile S.S. of Table I. Figures 8–10 present the absolute value of the product of the depth function for modes 1–5 as well as 10 at 1030 cps and modes 1–3 at 530 cps. This product is the initial mode amplitude—i.e., the mode amplitude before any range dependence is introduced. In the theoretical section, this product is indicated as a function of the dimensionless parameters l and l_0. Here, we present the product as a function of Z (the receiver depth) for a fixed source depth ($Z_0 = 55$ ft). (Since reciprocity holds, we may also regard Figs. 8–10 as giving the initial mode amplitudes as a function of source depth for a fixed receiver depth of 55 ft.) Each decade change in amplitude corresponds to a 20-dB change in intensity level.

Although Figs. 8–10 are for a fixed source depth, the mode curve for any other source depth (Z_0) can be obtained by a simple graphical translation of the dependent variable. This is possible because the dependent variable is plotted on a logarithmic scale. The procedure is based on the identity,

$$\log |U_n(Z)U_n(Z_0)| = \log |U_n(Z)U_n(55)|$$
$$+ \log |U_n(Z_0)U_n(55)|$$
$$- \log |U_n(55)U_n(55)|. \quad (27)$$

For a particular mode, one then measures the difference between the value for the receiver depth equal to the desired source depth and the value for the receiver depth equal to 55 ft. The entire mode curve is then translated by this difference.

In Figs. 8–10, the mode amplitudes are arbitrarily terminated near the surface. They do, in fact, go to zero at the surface as this is a boundary condition on the solution. Although the theoretical solutions above and below the channel depth have a different form, we

see that the depth functions as well as their slope are continuous at the channel depth. These are also boundary conditions on the solution. In this treatment, which follows Marsh, the condition for continuity of slope at the layer interface is equivalent to the eigenvalue equation. The other boundary conditions are satisfied by the general form of the solution, as can readily be seen by examination of Eqs. (2)–(4). However, the slope condition will be satisfied only if the eigenvalue equation is solved exactly. In early investigation of this mode theory, we were made aware of the inadequacy of approximate solutions to the eigenvalue equation by the fact that slope discontinuities appeared at the channel interface. (Furry's[1] treatment differs in that the eigenvalue equation is equivalent to the condition that the solution be zero at the surface.)

These mode patterns bear a striking resemblance to those associated with elementary-wave-motion problems. Note in all cases that mode n has n nulls (nodes) and n peaks (antinodes) above the channel depth. We have found this to be true in all of our investigations thus far, although it may not apply for all conditions. This feature has been of help in identifying mode numbers in complicated cases where approximate roots to the eigenvalue equation are unavailable. We allow the computer to find roots more or less by chance; the depth functions associated with these roots are computed and plotted; and the mode number is determined from the number of nulls or peaks appearing in the plot.
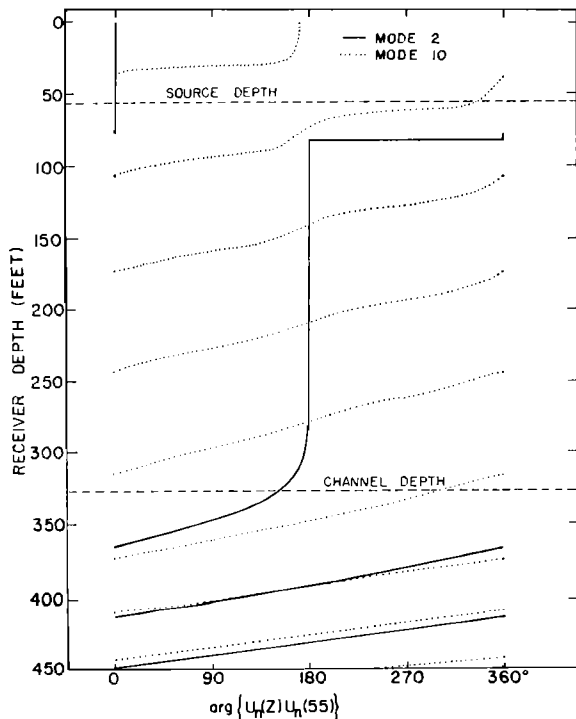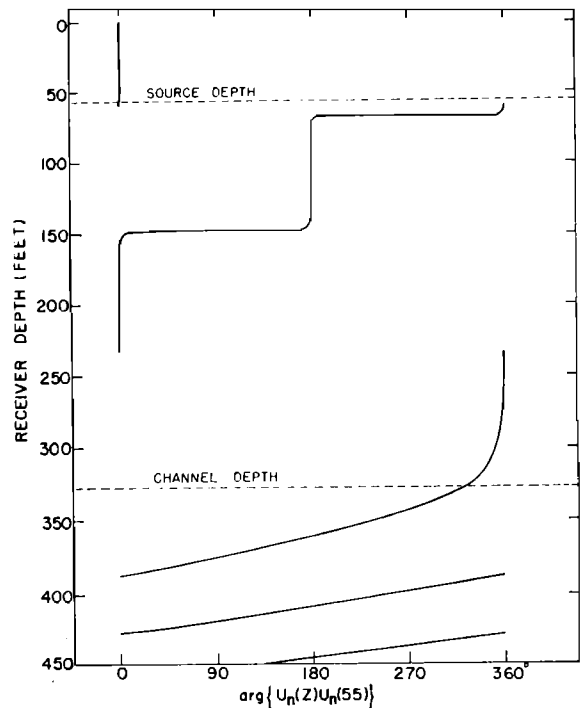

FIG. 12. Depth-function phase for mode 3 (1030 cps).

Thus, we can tell if any modes have been skipped and remain to be determined. Since the mode numbers are ordered by the magnitude of the eigenvalues, we then know in general where to look for the undetermined eigenvalues. For example, if mode 2 has been initially determined, then we need look for only one root that has a smaller real and a smaller imaginary part, i.e., the root for mode 1. Note that the amplitude at the successive peaks or nulls increases with increasing depth. We have found this to be true in other cases, although we have no proof that it will be true in general.

The mathematical explanation for the sharp nulls in Figs. 8–10 can best be treated in conjunction with a discussion of the initial mode phase. Values of this phase at 1030-cps frequency are shown for modes 2 and 10 in Fig. 11 and for mode 3 in Fig. 12. Values for mode 1, not shown here, lie within 0.1° of zero phase for receiver depths from the surface to a depth of about 265 ft. For low-order modes in the channel, the phase remains nearly constant at either 0° or 180° and changes rapidly but without discontinuity from one state to the other. The depths at which these changes occur correspond to the depths at which the nulls occur in Figs. 8–10. For example, in the case of mode 2 at 1030 cps, the phase changes by −178.8° and the mode amplitude varies through some 42 dB as the receiver depth is changed from 81 to 81.36 ft.

Let us now examine in more detail the mathematical nature of the solution for it indicates that the amplitude and phase patterns shown in Figs. 8–12 are characteristics of modes with small $\text{Im} M x_n$ (small damping).

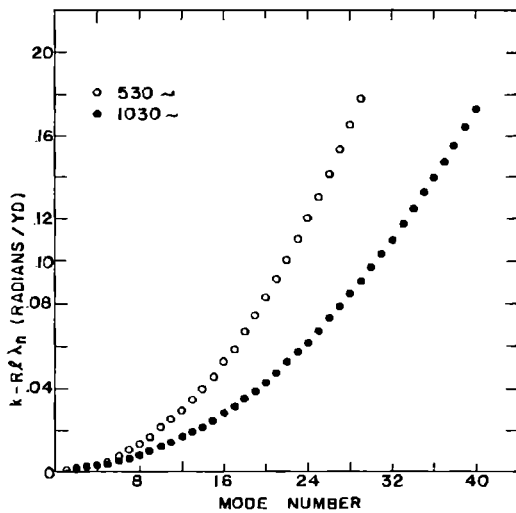FIG. 11. Depth-function phase for modes 2 and 10 (1030 cps).

FIG. 13. Real part of the complex wavenumber vs mode number.

For receivers in the channel, there are three factors that determine the phase: $A_n(t)$, $U_n(t_0)$, and D_n. The latter two factors determine a fixed phase shift, i.e., independent of receiver depth. Consider first the effect of source depth. The pattern for source depths other than 55 ft can be obtained by a simple translation based on the identity,

$$\arg\{U_n(Z)U_n(Z_0)\} = \arg\{U_n(Z)U_n(55)\}$$
$$+\arg\{U_n(Z_0)U_n(55)\}$$
$$-\arg\{U_n(55)U_n(55)\}. \quad (28)$$

Note that, for most source depths in the channel, the phase diagram for the low-order modes will either be the same as those given in Figs. 11 and 12 or will differ by 180°. The phase will, in general, again be either 0° or 180°, with exceptions occurring if the source is placed at critical depth where the phase is changing rapidly from one state to the other.

Although it is not demonstrated here, D_n is almost a pure negative real number for modes with small $\text{Im}Mx_n$.

The dependence on receiver depth is contained in the function $\mathcal{C}_n(t)$. We first note that $d\mathcal{C}_n(t)/dt$, evaluated at $t=0$, is equal to $-MW$. Where W is the Wronskian and is a negative pure imaginary constant. Since $\mathcal{C}_n(t)=0$, it follows then that $\arg\{\mathcal{C}_n(0)\}=90°$. This applies to all modes. In the case of modes for which $\text{Im}Mx_n$ is small, we can expand the h functions of $\mathcal{C}_n(t)$ in a Taylor series about the real part of the arguments and obtain the following general form:

$$\mathcal{C}_n(t) = if_n(t) + \text{Im}Mx_n g_n(t) + 0(\text{Im}Mx_n)^2. \quad (29)$$

Here, $f_n(t)$ and $g_n(t)$ are real functions. When $\text{Im}Mx_n$ is small, then $f_n(t)$ will generally be the dominant term and $\arg\{\mathcal{C}_n(t)\}$ is either 90° or 270°, depending on the sign of $f_n(t)$. As t is increased from zero, $f_n(t)$ starts out positive and changes sign $n-1$ times. The peaks and nulls in the interference pattern for practical purposes

correspond to the maxima and zeroes of $f_n(t)$. Note that the amplitude of $\mathcal{C}_n(t)$ at the nulls is proportional to $\text{Im}Mx_n$. This explains why the nulls become less prominent as the mode number is increased since $\text{Im}Mx_n$ increases with increasing mode number.

A. Complex Wavenumbers

Let us next examine in more detail the dependence of the mode solutions on the range variable for profile S.S. of Table I. In the computer program, the expression giving the range dependence $H_0^2(\lambda_n r)$ is calculated by an asymptotic expansion of many terms. However, as indicated in Eqs. (11)–(15), the essential behavior with range can be obtained by consideration of the complex wavenumber λ_n.

Since there is such a small difference between $\text{Re}\lambda_n$ and k, it is convenient to consider $k-\text{Re}\lambda_n$, which is the σ_n of Eqs. (11) and (14). Figure 13 presents σ_n as a function of mode number for frequencies of 530 and 1030 cps. $\text{Re}\lambda_n$ is slightly less than k for mode 1 and decreases as the mode number increases. Since σ_n increases with increasing mode number, from (14) we see that the higher the mode number, the more rapidly the phase angle of that mode increases with range.

Figure 14 presents the mode attenuation as a function of n. This mode attentuation is given by $-8686 \text{Im}\lambda_n$ dB/kyd. Values for the first two modes at 530 cps and the first four modes at 1030 cps, too small to indicate in Fig. 14, are, respectively, 7.44×10^{-3}, 3.17×10^{-1}, 6.61×10^{-7}, 5.75×10^{-4}, 3.71×10^{-2}, and 3.74×10^{-1} dB/kyd. These are the modes that propagate to relatively long ranges and that are referred to in the literature as trapped modes. A generally accepted condi-
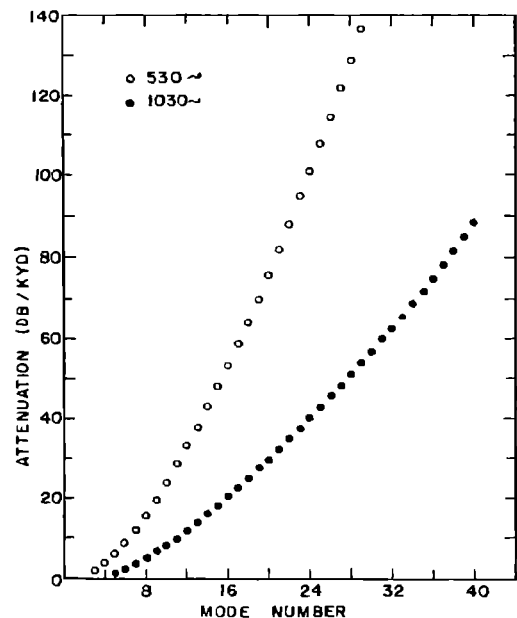

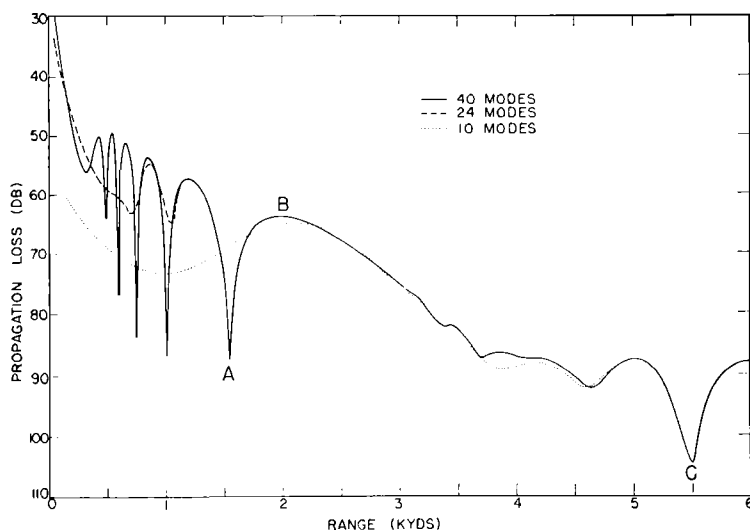FIG. 14. Mode attenuation vs mode number.

FIG. 15. Comparison of mode solutions obtained by including different numbers of modes (400-ft receiver, 1030 cps).

tion for trapping is that $Mx_n < M$. This condition, though convenient, is somewhat arbitrary since the onset of trapping for a particular mode is a continuous rather than a discrete process. In any case, the formerly held distinction between trapped and leaky modes is of small concern here since the leaky as well as the so-called trapped modes are included in the computations. For the condition of Fig. 14, the mode attenuation increases monotonically with mode number to as large as 136.5 dB/kyd for mode 29 at 530 cps and 88.2 dB/kyd for mode 40 at 1030 cps.

B. Vector Representation of Mode Contributions

Before examining in detail the nature of the mode combination that forms the image-interference pattern, consider how the number of modes included in the mode summation affects the resultant propagation loss. Figure 15 denotes the manner in which the inclusion of additional modes improves the mode solution. The three different lines represent the solution obtained by using different numbers of modes. At all ranges beyond 4.9 kyd, the three solutions agree to tenths of a decibel. The 10-mode solution is reasonably accurate beyond 2.3 kyd but departs markedly at shorter ranges. The 24-mode solution is accurate to 1.2 kyd. The 40-mode solution, which is identical to the dashed line in the upper part of Fig. 4, extends the familiar image-interference pattern in to somewhat less than 0.5 kyd. Comparison with ray theory indicates that the 40-mode solution is accurate in to a range of 550 yd.

In the mode theory, the basic dependence on range is cylindrical spreading with an additional attenuation term. The question then arises as to how this mode theory can be accurate in the image-interference region where the basic dependence on range is spherical spreading. The answer lies in the fact that the high attenuation of the high-order modes reduces their contribution very rapidly with range. Thus, at close range, the resulting propagation loss increases at a considerably greater rate than cylindrical spreading because of what is essentially a successive drop out of these high-order modes. At longer ranges, the contributions of these high-order modes is nil and the spreading is cylindrical with a relatively small attenuation term.

Figure 16 presents individual mode amplitudes in vector form with their resultants marked R. To be more specific, these vectors represent individual terms in the summation of Eq. (9) while the resultant represents the sum. The letters A to C refer to the range for which the terms were calculated. These ranges correspond to those similarly labeled in Fig. 15. A magnitude scale is indicated for each set with set C expanded to twice the scale of A and B. Modes not shown here make no essential contribution to the resultant. As can be seen in the mode-theory approach, the peaks and nulls of the image-interference pattern resul' from a much more complicated behavior than the relatively simple interaction between a source and its surface image as depicted by ray theory. For example, at range A, the amplitudes of modes 6–15 are all larger than that of the resultant. Investigation of Fig. 16 and other cases not shown here indicates that the peaks and nulls of the interference pattern are produced by a seemingly haphazard arrangement of vectors that amazingly reinforce or cancel each other at the proper ranges. It seems quite remarkable that the initial amplitudes and phase together with the attenuation and rate of change of phase operate for each mode in such a manner as to produce the image-interference pattern.

In discussing electromagnetic propagation, Furry[8] notes, ". . . completely trapped modes may exist separately, but leaky modes may not. The expansions of

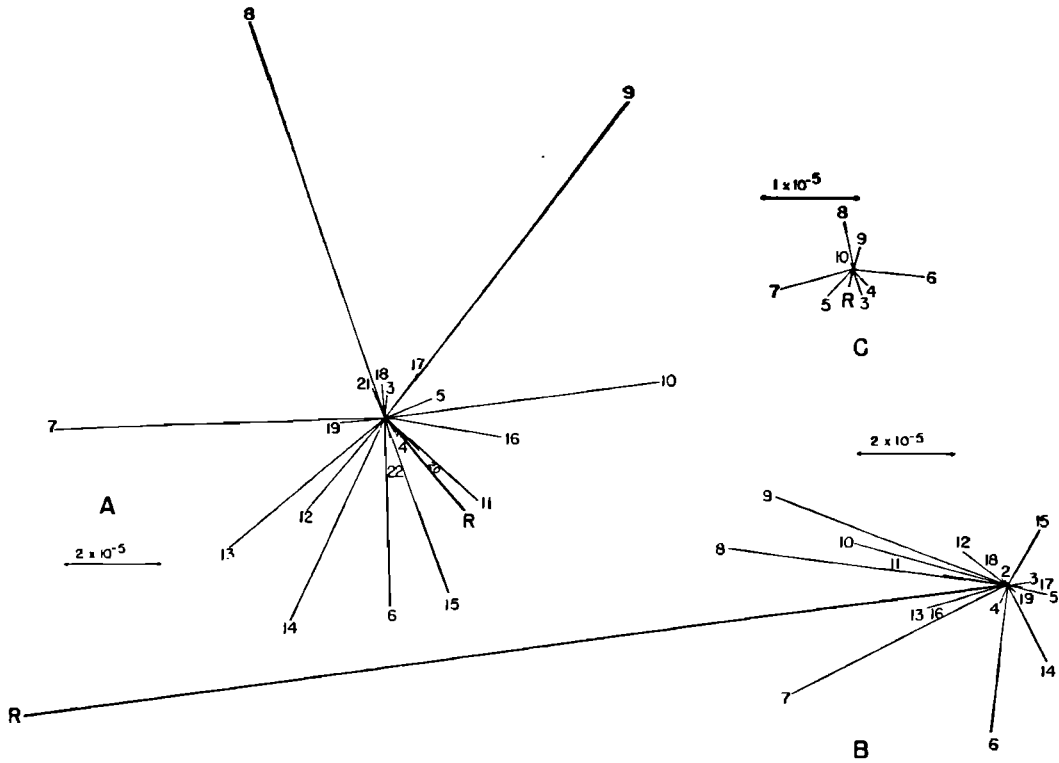[8] C. R. Burrows and S. S. Attwood, *Radio Wave Propagation* (Academic Press Inc., New York, 1949), p. 171.

Fig. 16. Vector representation of the mode contributions at the three ranges designated by letters in Fig. 15.

fields in terms of leaky modes are thus essentially mathematical." Perhaps, then, we should not expect a complete interpretation of individual modes from a physical standpoint. If the problem has been stated and solved properly, then the mathematical solution consisting of the mode summation must of necessity produce the interference pattern despite the fact that the interaction of individual modes appears physically inexplicable.

IV. SUMMARY

Comparison with ray theory and experimental results indicates that normal-mode theory for a bilinear surface duct can be successfully applied in the image-interference region. The propagation losses of both theoretical approaches are practically identical with the accuracy of the mode solution at very close ranges,

being limited only by the number of modes included in the computation. Comparison with experimental data indicates that the mode theory is superior to ray theory in the region where ray theory predicts shadow zones or caustics. Although the normal-mode solution faithfully reproduces the image-interference pattern, the process appears to be essentially mathematical and not amenable to a simple physical interpretation such as that inherent in the ray-theory approach.

ACKNOWLEDGMENTS